Tailored $(La_{0.2}Pr_{0.2}Nd_{0.2}Tb_{0.2}Dy_{0.2})_2Ce_2O_7$ as a Highly Active and Stable Nanocatalyst for the Oxygen Evolution Reaction

Sreya Paladugu, Ibrahim Munkaila Abdullahi, Palani Jothi, Bo Jiang, Manashi Nath, and *Katharine Page**

S. Paladugu, B. Jiang, Prof. K. Page
Department of Materials Science and Engineering, University of Tennessee, Knoxville, TN 37996, USA
Email Address: kpage10@utk.edu
P. Jothi
JTEC Energy, Atlanta, GA 30312, USA
I. M. Abdullahi, Prof. M. Nath
Department of Chemistry, Missouri University of Science and Technology, Rolla, Missouri 65409, USA

Keywords: *compositionally complex oxide, oxygen evolution reaction, mesoporous, nanocatalyst*

Designing highly active and robust catalysts for the oxygen evolution reaction is key to improving the overall efficiency of the water splitting reaction. We have previously demonstrated that evaporation induced self-assembly (EISA) can be used to synthesize highly porous and high surface area cerate-based fluorite nanocatalysts, and that substitution of Ce with 50% rare earth (RE) cations significantly improves electrocatalyst activity. Herein we further explore the defect structure of the best performing nanocatalyst in the series, $Nd_2Ce_2O_7$, with a combination of neutron diffraction and neutron pair distribution function analysis. It is found that Nd^{3+} cation substitution for Ce in the CeO_2 fluorite lattice introduces higher levels of oxygen Frenkel defects and induces a partially reduced $RE_{1.5}Ce_{1.5}O_{5+x}$ phase with oxygen vacancy ordering. Significantly, it is demonstrated that the concentration of oxygen Frenkel defects and improved electrocatalytic activity can be further enhanced by increasing the compositional complexity (number of RE cations involved) in the substitution. The resulting novel compositionally-complex fluorite– $(La_{0.2}Pr_{0.2}Nd_{0.2}Tb_{0.2}Dy_{0.2})_2Ce_2O_7$ is shown to display a low OER overpotential of 210 mV at a current density of 10 $mAcm^{-2}$ in 1M KOH, and excellent cycling stability. We suggest that increasing the compositional complexity of fluorite nanocatalysts expands our ability to tailor catalyst design.

1 Introduction

Electrochemical water splitting has been proposed as a sustainable approach to store electricity generated from intermittent renewable energy sources in the form of hydrogen fuel and reduce our reliance on fossil fuels.[1–4] Water splitting is composed of two half reactions: the oxygen evolution reaction (OER) and the hydrogen evolution reaction, which occur at the anode and cathode respectively.[3,5–7] The overall efficiency and large scale industrialization of the water splitting reaction is limited by the sluggish kinetics of the four electron-proton transfer process involved in OER.[8–10] Thus far, the benchmark electrocatalysts used to reduce the overpotential required for the OER have primarily comprised of precious metals and their oxides (Ru, Ir, RuO_2, and IrO_2).[11,12] Despite their high activity, the scarcity, high cost and instability of precious metal based oxides presents major drawbacks. In this context, contemporary research efforts have been directed towards the development of alternate highly active precious metal-free electrocatalysts for the OER.

Ceria based mixed oxides have shown promise for electrocatalysis applications, owing to ceria's abundance in natural reserves, excellent reduction and oxidation (redox) properties, and mechanical stability and corrosion resistance in alkaline environments.[5] The desirable redox properties of ceria arise from its ability to dynamically and reversibly convert between Ce(III) and Ce(IV), enabling the formation of oxygen vacancies and a defect rich structure.[13–15] Previous studies have demonstrated that introducing dopants into the host lattice of ceria is an effective materials design strategy to tune the electronic and defect structure of ceria, leading to favorable adsorption sites for reaction intermediates and enhanced OER activity.[5]

In our previous work, we demonstrated that cerate-based OER catalysts with high activity and stability can be achieved using the Evaporation Induced Self Assembly (EISA) synthesis route. Furthermore, the work revealed that 50% substitution of any one of the RE cations La, Pr, Nd, Tb, or Dy for Ce improved the electrocatalytic activity relative to a CeO_2 composition prepared by the same method. Among the rare earth cerate oxides examined, $Nd_2Ce_2O_7$ achieved the best activity (OER overpotential of 243 mV

at a current density of 10 $mAcm^{-2}$), and displayed modest stability under cycling in an alkaline medium. Crystal structure analysis, X-ray Photoelectron Spectroscopy (XPS) studies, and supporting Density Functional Theory (DFT) calculations across the series suggest the increased activity can be linked to large concentrations of oxygen vacancies and a redistribution of electronic structure in the host lattice, resulting in a decrease in OH* adsorption energy. OH* is a key reaction intermediate in OER and the presence of oxygen vacancies in OER catalysts has been demonstrated to enhance activity by promoting reaction intermediate adsorption.[16–18] Investigation into the nature and extent of oxygen vacancies present in EISA derived $Nd_2Ce_2O_7$ relative to CeO_2 is therefore of great interest.

Compositionally complex oxides (CCOs) are a class of multi-component oxides comprised of multiple cations on at least one distinct crystallographic lattice site. CCO is a more general class than the related High Entropy Oxides or Entropy Stabilized Oxides.[19] Although there is much debate about the precise definition of CCOs in the research community, CCOs are loosely defined as having a mixing configurational entropy of 1-1.5R (with R being the ideal gas constant) on at least one cation lattice site.[20,21] CCOs have attracted interest as promising OER catalysts due to observed instances of improved catalytic activity, lower overpotentials and longer-term stability compared to end-member compositions.[22,23] The improved OER activity of CCOs has been attributed to entropy stabilization and the synergistic effect of incorporating various catalytically active metal elements.[24] Additionally, the CCO platform can be used to introduce more structural defects and oxygen vacancies than known endmember oxide systems.[5,24]

In this work, we examine the effect of introducing Nd and multiple rare earth cations into the fluorite type host lattice of ceria on the nature and extent of oxygen vacancy structure, and intrinsic OER activity of the electrocatalyst. We use the CCO concept to design a new compositionally complex fluorite nanostructure within the class $RE_{0.5}M_{0.5}O_{2-x}$, where RE represents rare earth cations and M is cerium (Ce). Ceria, which has a fluorite type crystal structure, has been investigated as a co-catalyst or support for the OER, in combination with transition metals or noble metals.[5,25–27] Our prior work showed that partial substitution of Ce^{4+} with (mainly) trivalent RE cations can introduce oxygen vacancies into the lattice, reduce/ potentially eliminate the need for noble metal cations, and potentially promote the adsorption of oxygen containing intermediates in the OER. As shown in Figure 1, when RE cations are introduced into the fluorite lattice, the $Ce^{3+/4+}$ and RE cations randomly occupy the 4*a* Wyckoff position, while the oxygen anions occupy 7/8ths of the tetrahedral sites on position 8*c*. Doping CeO_2 with (mainly) lower valent RE^{3+} cations such as Pr, Nd, Dy and La is known to depress the concentration of Ce^{3+} and introduce large amounts of oxygen vacancies resulting in a defect fluorite structure.[14,15,28–31] Here, we again use a soft templating evaporation induced self-assembly approach (EISA) to synthesize OER fluorite catalysts with high surface area, porosity/nanoarchitecture, and varying degrees of compositional complexity, with the objective of increasing the number of exposed active sites and improving mass diffusion kinetics.[5] Furthermore, EISA is an inexpensive, highly tunable, and easily scalable synthesis approach, making it feasible for industrial manufacturing.

Using the EISA approach, fluorite samples with nominal compositions: CeO_2, $Nd_2Ce_2O_7$ and $(La_{0.2}Pr_{0.2}Nd_{0.2}Tb_{0.2}Dy_{0.2})_2Ce_2O_7$ (hereafter referred to as $RE_2Ce_2O_7$) were synthesized at various calcination temperatures to find optimized reaction conditions and determine the effect of incorporating a single RE cation and multiple RE cations in a compositionally complex configuration on the OER activity of fluorite nano electrocatalysts. The phase purity and morphology of the samples are examined with X-ray diffraction, Brunauer-Emmett-Teller (BET) and Scanning Electron Microscopy (SEM) studies. X-ray Photoelectron Spectroscopy (XPS) is used to determine surface valence states. Raman spectroscopy and neutron total scattering analysis are applied to study the nature and correlation length scale of oxygen vacancies in the series. Linear sweep voltammetry (LSV) measurements and chronoamperometry stability measurements are performed in a 1M KOH electrolyte to examine electrocatalytic activity and stability and link structure-property effects with the extent of compositional substitution.

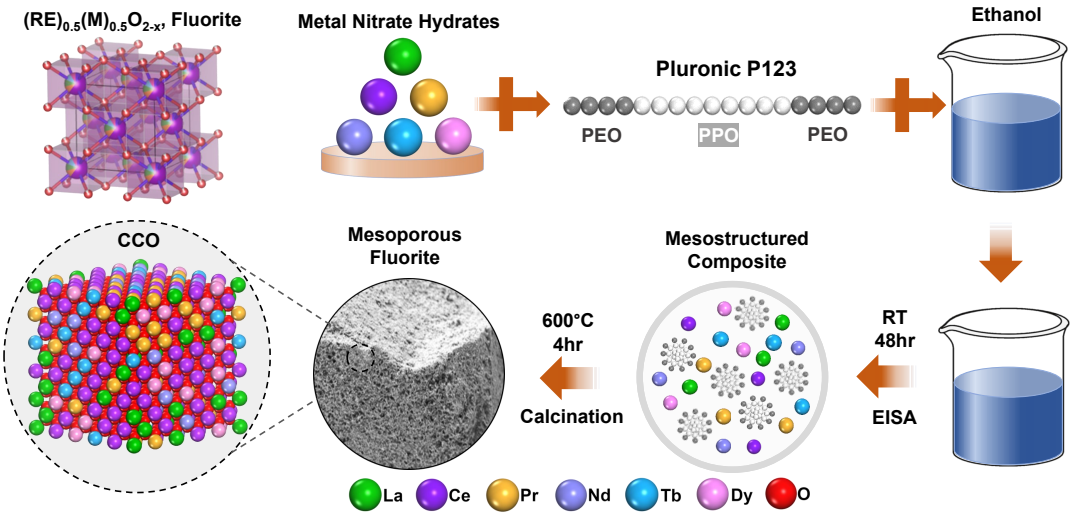

Figure 1 Synthesis schematic of mesoporous fluorite catalysts using a soft templating strategy via Evaporation Induced Self Assembly (EISA); calcination temperatures between 400°C and 1000°C are used in this work. The fluorite unit cell is shown on the top left with VIII-fold cation coordination polyhedron depicted as purple cubes with red O atoms at the vertices. The cation sites are occupied, on average, with equal parts of 5 RE ions and 1 M ion. When the fluorite A site is doped with a trivalent (+3) species, a multivalent cation like Ce is reduced from a +4 to a +3 state, and charge compensation occurs through point defects on the oxygen lattice sites resulting in a defect fluorite structure where Ce is VII-fold coordinated with oxygen. The CCO with a defect-fluorite structure can be written as $RE_{0.5}M_{0.5}O_{2-x}$.

2 Results and Discussion

2.1 Structure and Morphology

CeO_2, $Nd_2Ce_2O_7$ and $RE_2Ce_2O_7$ were synthesized using EISA as detailed in Section 4.2.1 and illustrated in Figure 1, at 400°C, 600°C, 800°C and 1000°C to find the optimal calcination temperature for the OER. The structure of the samples was investigated using powder X-ray diffraction (XRD) as shown in Figure 2 and the morphology and sample homogeneity was determined using Scanning Electron Microscopy (SEM) and Energy Dispersive X-ray Spectroscopy (EDS) as seen in Figure 2 f and i.

XRD was performed to determine the phase purity and crystallinity of the samples with increasing calcination temperature, as seen in Figure 2 (a), (d) and (g). XRD patterns of all samples as prepared at 400 °C, display peak broadening indicative of the highly nanocrystalline nature of samples produced using the low temperature EISA synthesis route. Interestingly, samples containing RE cations appear less crystalline than those with CeO_2 composition, at all calcination temperatures. As the calcination temperature increases, the Bragg peaks become progressively narrower, indicating enhanced crystallinity, which can be attributed to particle growth. It is notable that at 800 °C and 1000 °C, $RE_2Ce_2O_7$ and $Nd_2Ce_2O_7$ display significantly broader diffraction peaks than CeO_2 possibly due to greater intrinsic disorder and/or smaller crystalline grain size resulting from sluggish diffusion kinetics.

CeO_2 and $RE_2Ce_2O_7$ samples form an average cubic fluorite structure at all calcination temperatures, with no evidence of secondary phases. $Nd_2Ce_2O_7$ was found to form an average cubic fluorite structure up to calcination temperatures of 800 °C. At 1000 °C, the formation of superstructure peaks is observed, indicated by the blue stars in Figure 2 (d). Rietveld refinement of the CeO_2 sample was performed successfully using an ideal fluorite structure with cubic space group (S.G.) $Fm\bar{3}m$. In the cubic structure, the Ce ions occupy the 4*a* Wyckoff position and have eight-fold coordination with oxygen ions, which occupy the 8c tetrahedral Wyckoff position. In the ideal fluorite structure, the oxygen sub lattice is fully occupied. The average structure of $Nd_2Ce_2O_7$ up to 800°C and $RE_2Ce_2O_7$ at all calcination temperatures, was modeled successfully with a single phase defect fluorite structure, indexed to space group (S.G.) $Fm\bar{3}m$, with RE and Ce cations randomly occupying 4*a* sites and oxygen anions occupying 7/8ths of 8*c* sites.[32,33] Representative Rietveld refinement results for the samples calcined at 600°C are shown in Figure 2 (c).

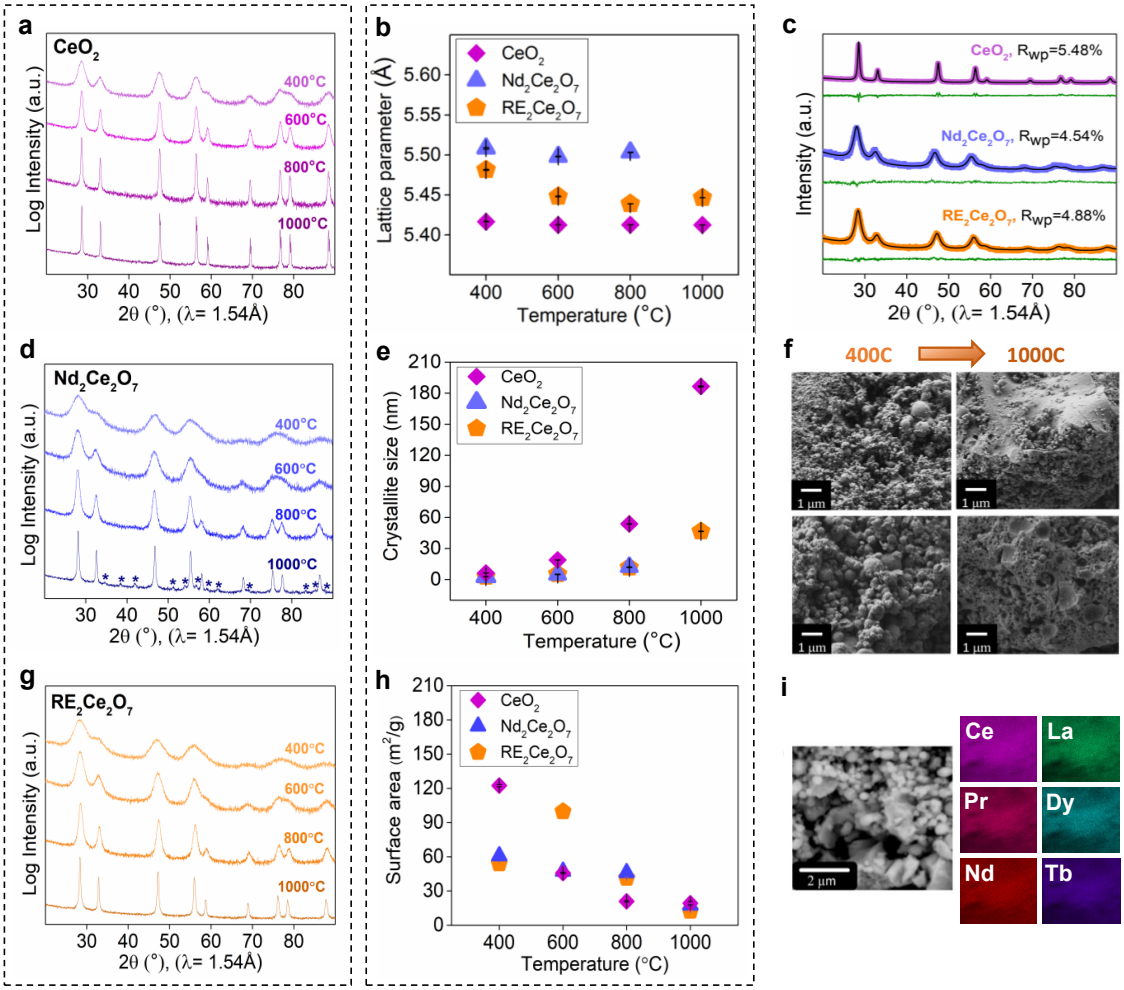

Figure 2 XRD patterns of CeO_2, $Nd_2Ce_2O_7$ and $RE_2Ce_2O_7$ shown in (a),(d) and (g) respectively, prepared by calcination at 400°C, 600°C, 800°C and 1000°C (from top to bottom of each panel). The XRD pattern of $Nd_2Ce_2O_7$ calcined at 1000 °C shows the formation of super-structure peaks as indicated by the blue stars. Refined values from Rietveld refinements of data for CeO_2 (purple), $Nd_2Ce_2O_7$ (blue) and $RE_2Ce_2O_7$ (orange) are shown for (b) lattice parameter, (e) crystallite size and (h) BET surface area. Rietveld refinement results of XRD data of samples prepared by calcination at 600°C are shown in (c), where the data was fit to a cubic phase with S.G. $Fm\bar{3}m$ for CeO_2, $Nd_2Ce_2O_7$ and $RE_2Ce_2O_7$. Measured data are shown as colored circles, structural model fits as a black line through the data, and the difference curves in green fall below the data and fits. (f) Scanning Electron Microscopy (SEM) images of $RE_2Ce_2O_7$ prepared by calcination at 400°C for 4 hours (shown in the column on the left) and 1000°C for 4 hours (shown in the column on the right).(i) SEM image (left) and corresponding EDS spectra maps (right, in color) for $RE_2Ce_2O_7$ prepared by calcination at 400°C for 4 hours. A region displaying heterogeneous morphology (larger flakes and smaller spheres) was intentionally selected.

The $Nd_2Ce_2O_7$ sample calcined at 1000°C forms a cubic C-type (bixbyite) structure with space group $Ia\bar{3}$ as shown by the Rietveld refinement in SI Figure S1. The presence of this cubic C-type structure in rare-earth containing cerates has been widely reported in literature.[14,34–38] The C-type structure is related to the fluorite structure but exhibits oxygen vacancy ordering resulting from the selective removal of 25% of the oxygen anions.[34,38] Whereas the cations in the fluorite structure are 8-fold coordinated with oxygen, the cations in the C-type structure are 6-fold coordinated and occupy the 8*b* and 24*d* Wyckoff sites with the O anions occupying the 48*e* sites. Interestingly, while the $Nd_2Ce_2O_7$ sample calcined at 1000°C displays a C-type structure, the $RE_2Ce_2O_7$ sample retains a defect fluorite structure at all calcination temperatures. It appears that the incorporation of five RE cations into the defect fluorite phase has inhibited the formation of the C-type structure, potentially making it a more stable catalyst than $Nd_2Ce_2O_7$.

Extracted parameters from Rietveld refinement provide further insights into structural trends across the series. As seen in Figure 2 (b), inclusion of RE^{3+} cations results in a lattice expansion. In an ideal fluorite structure, Ce^{4+} cations are VIII-fold coordinated with oxygen; however, introducing (mainly) RE^{3+} cations into the fluorite lattice results in partial conversion of Ce^{4+} to Ce^{3+} and a change in cation coordination from VIII-fold to VII-fold. The increase in lattice parameter upon inclusion of RE^{3+} cations is due to the larger ionic radius of La^{3+} (1.1 Å), Nd^{3+} (1.046 Å), Pr^{3+} (1.058 Å), Tb^{3+} (0.98 Å) and Dy^{3+} (0.97 Å) relative to Ce^{4+} (0.92 Å) in VII-fold coordination. The ionic radii for VII-fold coordination were calculated as an average of ionic radii for VI and VIII fold coordination.[39–41] Tb, Dy and Pr are known to form mixed 3+ and 4+ valence states.[14,38,38,42]

No significant changes were observed in lattice parameter with increasing calcination temperature, suggesting that oxygen stoichiometry remains consistent with increased calcination temperature (lattice expansion is a noted side effect of oxygen sub-stoichiometry in ceria and related compounds).[43–45]

The thermal stability of the fluorite samples with increasing calcination temperature was explored by extracting trends in crystallite size, shown in Figure 2 (e). Interestingly, samples containing RE cations display less dramatic crystallite size growth than CeO_2 samples with an increase in calcination temperature. Samples with 1 RE constituent cation exhibit similar crystallite size growth behavior compared to those with 5 RE constituent cations.

In addition to the structure of a catalyst, surface area and morphology are important parameters that can significantly influence catalytic activity by affecting accessibility to active sites, the number of exposed active sites and mass transfer limitations. BET surface area is a measure of the total surface area of a material, including both the electrochemically active and inactive regions. BET was used to measure the surface areas of the sample series as displayed in Figure 2 (h) and SI Figure S2. BET surface areas of the samples were found to be highly dependent on composition and calcination temperature. Typically, in nano oxide catalysts, increasing calcination temperature leads to particle size growth/coarsening and a corresponding decrease in BET surface area. Interestingly, the CCO composition in the series shows an anomalous increase in surface area when the calcination temperature of the sample is increased from 400°C to 600°C, followed by a decrease in surface area at calcination temperatures beyond 600°C. Other compositions show a decrease in surface area with increasing calcination temperature. The calcination series was repeated multiple times for each composition, and the trends were reproducible.

To further elucidate the surface area trends observed, the morphology of the $RE_2Ce_2O_7$ sample was studied as a function of increasing calcination temperature. As seen in Figure 2 (f) the sample was found to be highly heterogeneous, with a large particle size distribution and the presence of at least two distinct morphologies: (i) micrometer scale porous flakes and (ii) spherical nanoparticle agglomerates, similar to CCO morphologies reported by Cong et al.[46] With increasing calcination temperature, Ostwald ripening occurs resulting in larger but fewer spherical nanoparticles and an overall decrease in BET surface area. At higher calcination temperatures, the morphology is dominated by micrometer sized flakes with smaller, and more closed (less accessible) pores. The same overall trends in morphology as a function of increasing calcination temperature were observed in $Nd_2Ce_2O_7$ and CeO_2. However, the distinct BET surface area trends of $RE_2Ce_2O_7$, $Nd_2Ce_2O_7$ and CeO_2 suggests that the greater compositional complexity and more sluggish diffusion in the CCO sample may give rise to complex mor-

phology/growth patterns that can potentially be further optimized with thermal processing.
EDS measurements were performed on the $RE_2Ce_2O_7$ sample to investigate the formation of a solid solution. Elemental mapping, shown in Figure 2 (i) confirmed the homogeneous distribution of all elements present (La, Pr, Dy, Tb, Nd, Ce and O) at the micron scale. Spectra were collected for various particle morphologies across sample locations to confirm that the different morphologies possess the same chemical composition and distribution. Atomic ratios of RE cations to Ce as measured using EDS and X-ray Fluorescence (XRF) are displayed in SI Table S1. While several atomic percent error can be encountered with these methods, the analysis overall indicates compositions were found to closely resemble the target stoichiometry with minor deviation.

2.2 Defect Chemistry

Oxygen vacancies have been shown to increase adsorption of oxygen containing intermediates in the OER and enhance catalytic activity.[16–18] The effects of introducing rare earth cations on the defect chemistry of the fluorite catalyst series were evaluated as shown in Figure 3 using Raman spectroscopy (a, d and g), neutron total scattering (b, e and h), and X-ray photoelectron spectroscopy (XPS) (c, f and i). Raman spectroscopy was used to characterize the defect modes present in the sample series. As seen in Figure 3 (a), the Raman spectra of CeO_2 prepared by calcination at various temperatures shows a single Raman peak at 463 cm^{-1}. This peak can be ascribed to the first-order mode of F2g and corresponds to the Ce−O symmetric stretching of the CeO_8 vibrational unit in CeO_2.[47,48] An increase in the calcination temperature is accompanied by a decrease in the bandwidth of the first order mode of F2g with peak at 463 cm^{-1}. Such an observation has been attributed to an increase in particle size in previous literature reports.[47,48]
As shown in Figures 3 (d) and (g), $Nd_2Ce_2O_7$ and $RE_2Ce_2O_7$ exhibit D-band peaks at 580 cm^{-1} Raman shift. The D-band for $Nd_2Ce_2O_7$ samples calcined at 400°C and 600°C is split into D1 centered at 558 cm^{-1} and D2 centered around 607 cm^{-1}. The D band splitting is influenced by the concentration of Nd^{3+} as well as calcination temperature. An increase in the calcination temperature leads to a blue-shift of the D-band in $RE_2Ce_2O_7$ and $Nd_2Ce_2O_7$. This shift is more obvious in $Nd_2Ce_2O_7$ indicating a higher degree of local distortion in the lattice, perhaps due to its slightly expanded lattice.[49] The Raman spectra of both samples show a defect-induced Raman D-band and a second-order transverse acoustic (2TA) mode at 580 and 253 cm^{-1} which arise from the presence of oxygen vacancies and single or multiple RE dopant cations.[50] The highly pronounced D-band observed in $RE_2Ce_2O_7$ compared to $Nd_2Ce_2O_7$ comes from the defects-induced by multiple RE metal doping. Similar Raman spectra have been reported in metal doped ceria oxides.[47,49,51] Furthermore, a very small overtone peak of longitudinal optic (LO) mode at 2 LO (1080 cm^{-1}) was observed, characteristic of relaxation of multi-phonon by Raman resonance effect. However, the LO mode is less sensitive to defects relative to the D-band. Based on Raman Spectroscopy analysis $RE_2Ce_2O_7$ is found to display the highest amount of defect concentration relative to the other fluorite compositions in the series, as indicated by the intensities of the D-band. Additionally, $RE_2Ce_2O_7$ calcined at 600°C displays the highest surface area, and trends in lattice parameter and crystallite size with higher calcination temperature indicate that the composition displays improved thermal stablility relative to CeO_2.
In our examination of OER activity as a function of calcination temperature, we discovered that CeO_2, $Nd_2Ce_2O_7$ and $RE_2Ce_2O_7$ calcined at 600°C-exhibited the highest OER activity, as evidenced by their lowest overpotential values (SI Figure S3). Importantly, upon inspecting SI Table S2-4 we find that a high surface area does not directly correlate with enhanced OER activity across all compositions studied. For instance, $RE_2Ce_2O_7$ calcined at 1000°C displays a low BET surface area of 13 m^2/g and overpotential of 240mV; yet, it displays higher OER activity than CeO_2 calcined at 400°C with a surface area of 122 m^2/g and overpotential of 640 mV. These findings suggest that within the fluorite series, the chemical composition and inherent chemical activity are more decisive factors in catalytic performance than the BET surface area. As fluorite catalysts calcined at 600°C present the most promise as OER catalysts, all compositions calcined at 600°C were investigated further to determine the role of RE cations on OER catalytic performance.
To probe the nature of oxygen vacancies in both the average and local structure of the fluorite series,

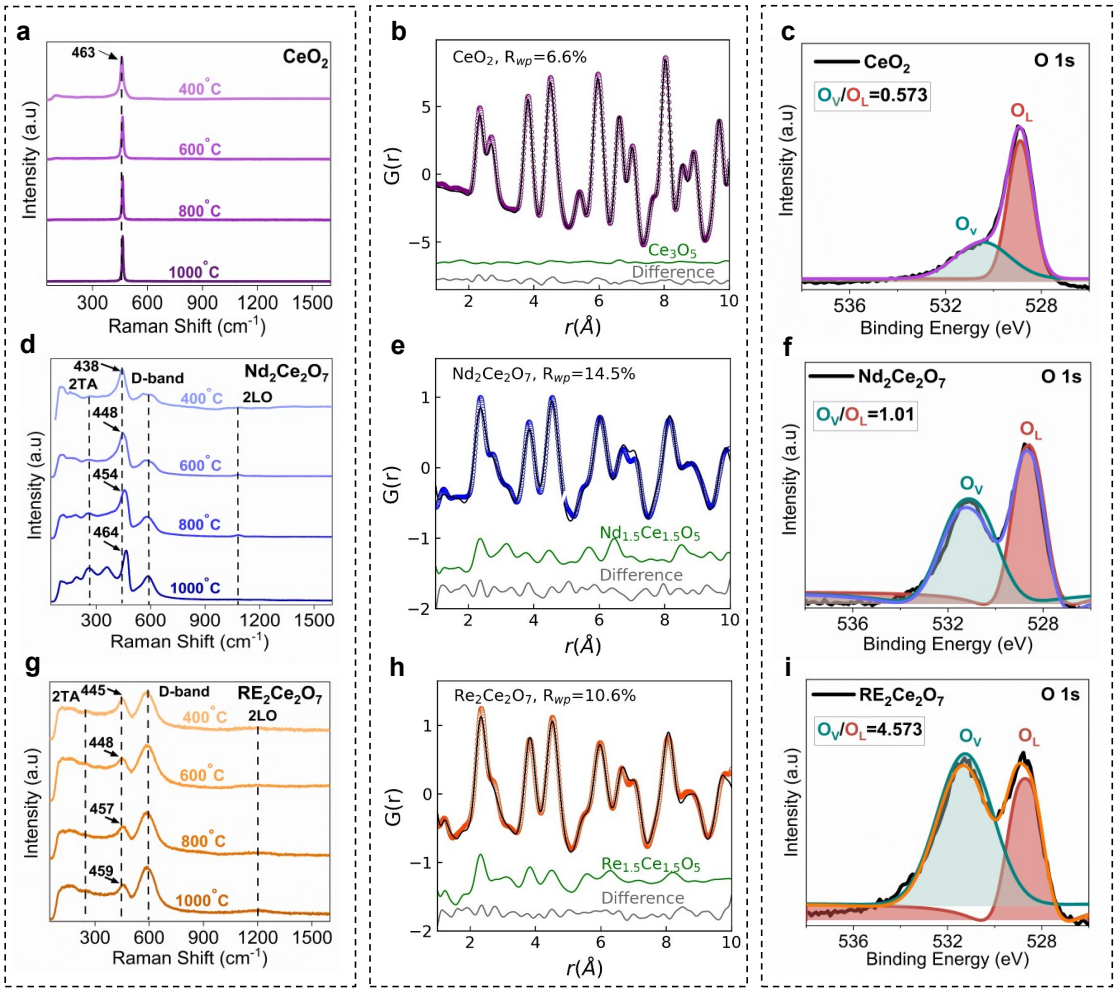

Figure 3 Raman, neutron PDF and XPS results for fluorite catalysts prepared by calcination at 600°C where the top row represents CeO_2, the middle row shows $Nd_2Ce_2O_7$ and the bottom row represents $RE_2Ce_2O_7$. Raman spectra (λ_{ex} = 632.8 nm) are shown in the panel on the left as (a), (d) and (g). 2-10Å neutron PDF refinements using a two phase model comprising of Frenkel-type defects with S.G. $Fm\bar{3}m$ and $Pnn2$- type Ce_3O_{5+x} for CeO_2, $Nd_{1.5}Ce_{1.5}O_{5+x}$ for $Nd_2Ce_2O_7$ and $RE_{1.5}Ce_{1.5}O_{5+x}$ for $RE_2Ce_2O_7$ are shown in the panel in the middle as (b), (e) and (h). The measured PDF data is shown as colored circles, the structural fit as a black line through the measured data and the difference curve in gray falls below the measured data and fits. The curve in green represents the phase contribution of the $Pnn2$- type Ce_3O_{5+x} phase. High resolution XPS O 1s core level binding energy spectra are shown in the panel on the right in (c), (f) and (i) where the area ratios of vacancy-related (O_V ,green) and lattice-related (O_L , red) oxygen are computed.

neutron total scattering analysis (Bragg diffraction, pair distribution function) was employed. Neutron diffraction and PDF have previously shown great sensitivity to the nature and length scale of oxygen vacancy correlations in catalysts[17,52,53], being more sensitive probes of oxygen atoms relative to x-ray techniques. Rietveld refinements were performed on the neutron diffraction data for the fluorite samples calcined at 600°C as shown in SI Figure S4 with the corresponding refined parameters shown in SI Table S5. Rietveld refinements indicate that CeO_2 exhibits an ideal fluorite average structure with S.G. $Fm\bar{3}m$. $Nd_2Ce_2O_7$ and $RE_2Ce_2O_7$ were successfully fit to a defect fluorite structure with S.G. $Fm\bar{3}m$ containing oxygen Frenkel defects, which have been widely observed in CeO_2-based materials.[14,32,33,52] Thus, neutron diffraction refinements reveal that incorporating RE cations into the host lattice of CeO_2, leads to the formation of Frenkel-type oxygen defects in the average structure.

To explore any deviation in the local oxygen vacancy structure of the fluorite series, the average structure models from neutron diffraction were applied to refinements of the neutron pair distribution functions (PDF) from 1.5-30 Å. The intermediate range PDF refinements are shown in SI Figure S5 with the corresponding refined parameters displayed in SI Table S6. In the case of CeO_2, the fluorite structure is able to accurately model the intermediate range; however, applying the average defect fluorite structure model to PDF refinements of $Nd_2Ce_2O_7$ and $RE_2Ce_2O_7$ results in significant discrepancies in fit below 10 Å as indicated by the high R_{wp} values of 24.01% and 21.15%, respectively.

The distinct local structures of $Nd_2Ce_2O_7$ and $RE_2Ce_2O_7$ were further investigated by performing PDF analysis of the low r-range as shown in Figures 3 (b), (e) and (h) respectively. Various single and two phase structural models were explored during refinements, including the Frenkel type defect structure and C-type bixbyite structure. $Nd_2Ce_2O_7$ was successfully fit to a two phase structural model comprising of a primary cubic phase with S.G. $Fm\bar{3}m$ containing oxygen Frenkel defects and a secondary oxygen vacancy ordered $Nd_{1.5}Ce_{1.5}O_{5+x}$ (1/6th oxygen vacancy) phase with orthorhombic S.G. *Pnn*2 which has been previously observed in CeO_2 nanorods.[52] $RE_2Ce_2O_7$ and CeO_2 were fit using the same two phase model as $Nd_2Ce_2O_7$ but with the stoichiometry- $RE_{1.5}Ce_{1.5}O_{5+x}$ (where RE = La, Nd, Tb, Dy and Pr) and Ce_3O_{5+x} respectively, in the secondary phase. As shown in SI Table S7, when CeO_2 is fit using this two phase structural model, a negligible 0.08% phase fraction of oxygen vacancy ordered Ce_3O_{5+x} is found. However, when RE cations are introduced into the host lattice of CeO_2, the phase fraction of the local oxygen vacancy ordered phase- $Nd_{1.5}Ce_{1.5}O_{5+x}$ in $Nd_2Ce_2O_7$ and $RE_{1.5}Ce_{1.5}O_{5+x}$ in $RE_2Ce_2O_7$, increases significantly. Importantly, while $Nd_2Ce_2O_7$ and $RE_2Ce_2O_7$ have a similar local oxygen stoichiometry, $Nd_{1.5}Ce_{1.5}O_{5+x}$ has a larger d(*Pnn*2) of 19nm than $RE_{1.5}Ce_{1.5}O_{5+x}$ (12.5nm) indicating that the oxygen vacancy ordered phase has a longer correlation length scale in $Nd_2Ce_2O_7$. Furthermore, the $RE_{1.5}Ce_{1.5}O_{5+x}$ phase appears to have a larger contribution in the low-r region (<5 Å) in $RE_2Ce_2O_7$ suggesting that it has a shorter length scale and is more disordered relative to $Nd_{1.5}Ce_{1.5}O_{5+x}$. Significantly, there is an increased concentration and longer correlation length scale of Nd/$RE_{1.5}Ce_{1.5}O_{5+x}$ in $Nd_2Ce_2O_7$ and $RE_2Ce_2O_7$ relative to the Ce_3O_{5+x} phase in CeO_2. The correlation length scale of oxygen vacancies has been shown to strongly influence the redox properties and resulting catalytic performance of ceria-based mixed oxides[53] and OER catalysts in general[17].

XPS was used to further examine the variation in oxygen defect chemistry of these samples and determine the valence states of the elemental constituents present on the surface of the fluorite catalysts. The wide scan survey spectra of all the samples in the series confirmed the coexistence of their respective constituent elements on their surfaces (SI Figure S6). The high- resolution La 3d spectrum of $RE_2Ce_2O_7$ shown in SI Figure S7 (a), exhibits regular doublet splitting which is further deconvoluted into four peaks (two peaks per doublet).The peaks at 834.5 eV and 851.4 eV, correspond to spin orbital 3d5/2 and 3d3/2 respectively, while the peaks at 838.3 eV and 855.6 eV, are satellite peaks ascribed to 3d5/2 and 3d3/2 respectively.[54] These peaks correspond to La–O_2 as supported by previous reports.[55]

The high- resolution Ce 3d spectra of $RE_2Ce_2O_7$, $Nd_2Ce_2O_7$ and CeO_2 are highly comparable (SI Figures S6 (b), S7 (a) and S8 (a) respectively) and all exhibit multiplet splitting, comprising six identical peaks at 882.1 eV, 888.4 eV and 897.9 eV for 3d5/2 and 990.5 eV, 906.8 eV and 916.3 eV for 3d3/2. These peaks confirm the presence of Ce(III) and Ce(IV) oxidation states in all the fluorite samples.[56–58]

The high-resolution Pr 3d spectrum of $RE_2Ce_2O_7$ (SI Figure S7 (c)) shows two doublets corresponding

to 3d5/2 and 3d3/2 at 932.8 eV and 953.4 eV with satellites at 928.4 eV and 984.2 eV respectively, indicating the presence Pr(III), in agreement with the preferential trivalent state of most RE-ions.[28] The observed satellites at a slightly lower binding energy are ascribed to the well-probed 4f3 final state.[59,60] The presence of Nd was confirmed in both $RE_2Ce_2O_7$ and $Nd_2Ce_2O_7$ from the high resolution Nd 3d spectra (SI Figures S7 (d), S9 (b)). The spectra show two doublets at 977.8 eV and 982.3 eV corresponding to a satellite and Nd(VI) of 3d5/2, and satellites at 1000.1 and 1004.7 eV corresponding to Nd(III) of 3d3/2[29,30]. The 4d spectra of $RE_2Ce_2O_7$ and $Nd_2Ce_2O_7$ shown in SI Figures S7 (e) and S9 (c) display peaks at 121.1 eV and 124.3 eV corresponding to a satellite and 4d.[28] The presence of Tb in the high-resolution Tb 3d spectrum of $RE_2Ce_2O_7$ (SI Figure S7 (f)) was confirmed by the presence of two characteristic doublet peaks for 3d5/2 and 3d3/2 and their corresponding satellites at 1241.0 eV, 1276.0 eV, 1251.4 eV and 1287.0 eV respectively. These characteristic peaks indicate the presence of Tb(IV) in agreement with literature reports.[61,62] Dy 3d spectrum of the $RE_2Ce_2O_7$ (SI Figure S7 (g)) shows doublet peaks due to the spin−orbit splitting at 1296.4 eV, and 1334.4 eV corresponding to Dy(III) of 3d3/2 and 3d5/2 respectively.[31,63] The satellite peak at 1303.9 eV is assigned to Dy(IV) 3d5/2 components, indicating the presence of mixed Dy ion states on the surface.[63]

As seen in Figure 3 (c), (f) and (i), the high-resolution O 1s XPS spectra for all fluorite samples were deconvoluted into two main peak components: oxygen vacancies (O_V), and lattice oxygen (O_L). The peak at 530.9 eV corresponds to a loosely absorbed oxygen species (correlated to oxygen vacancies). The O_L binding peak at 528.8 eV for each sample was associated with typical metal-oxygen bonding of lattice oxygen,[64] while O_V peak at 531.5 eV was attributed to the presence of surface chemisorbed oxygen associated with defects (oxygen vacancies).[64,65] The area ratio of O_V/O_L has been employed as a metric for estimating the proportion of surface oxygen vacancies, with higher ratios suggesting larger amounts of surface oxygen vacancies.[66] The larger concentration of surface oxygen vacancies in $RE_2Ce_2O_7$ facilitates the pre-oxidation of RE sites, increases hydroxyl adsorption and promotes the reconstruction of the defective surface with applied potential,[54,67] consequently improving OER performance.

2.3 Catalytic performance for the Oxygen-Evolution Reaction

The electrocatalytic behavior of the fluorite samples for the OER was studied using a three-electrode system, in a 1 M KOH alkaline solution. Fluorite samples synthesized at different calcination temperatures were tested to determine their catalytic activity towards OER. Among all compositions, samples calcined at 600°C showed optimal catalytic activity and hence these samples were pursued for further study. Polarization plots obtained from linear sweep voltammetry (LSV) of CeO_2, $Nd_2Ce_2O_7$ and $RE_2Ce_2O_7$ synthesized at 600°C, measured using a scan rate of 10 mV s^{-1}, are shown in Figure 4 (a). $RE_2Ce_2O_7$ demonstrated an exceptionally low overpotential of 210 mV attained at a current density of 10 mV s^{-2} and exhibited higher catalytic activity than the $Nd_2Ce_2O_7$ and CeO_2 samples, which showed overpotentials of 243 mV, and 347 mV respectively (Figure 4 (b)). The intrinsic OER activity of these catalysts can be ranked as follows ranging from highest to lowest activity: $RE_2Ce_2O_7$ > $Nd_2Ce_2O_7$ > CeO_2. Consequently, $RE_2Ce_2O_7$ is determined to be the best electrocatalyst in this series as it displays the highest intrinsic catalytic activity. It is important to note that the overpotential observed for the CeO_2 (347 mV) sample synthesized using EISA in this study, outperforms pristine CeO_2 OER electrocatalysts previously reported in literature[50,68,69] (relative comparison shown in SI Table S8). This suggests that EISA is a promising synthesis route for producing highly active OER catalysts relative to other synthesis approaches.

Cyclic voltammetry (CV) of all samples exhibit pre-oxidation peaks indicating oxidation of the active metal sites (SI Figure S10). $RE_2Ce_2O_7$, $Nd_2Ce_2O_7$ and CeO_2 show pre-oxidation peaks at 1.433, 1.349 and 1.381 V vs RHE at 10 mV/s scan rate respectively arising from Ce(III)/Ce(IV) contributions. The pre-oxidation peaks are more pronounced with variations in scan rate. The shift in the oxidation peak potential of $RE_2Ce_2O_7$ and $Nd_2Ce_2O_7$, relative to CeO_2, indicates the electronic perturbation effect resulting from the addition of a single/ multiple RE cation(s). The Tafel plots generated from LSV curves, were employed to evaluate the OER kinetics of the electrocatalysts. As displayed in Figure 4 (d), $RE_2Ce_2O_7$

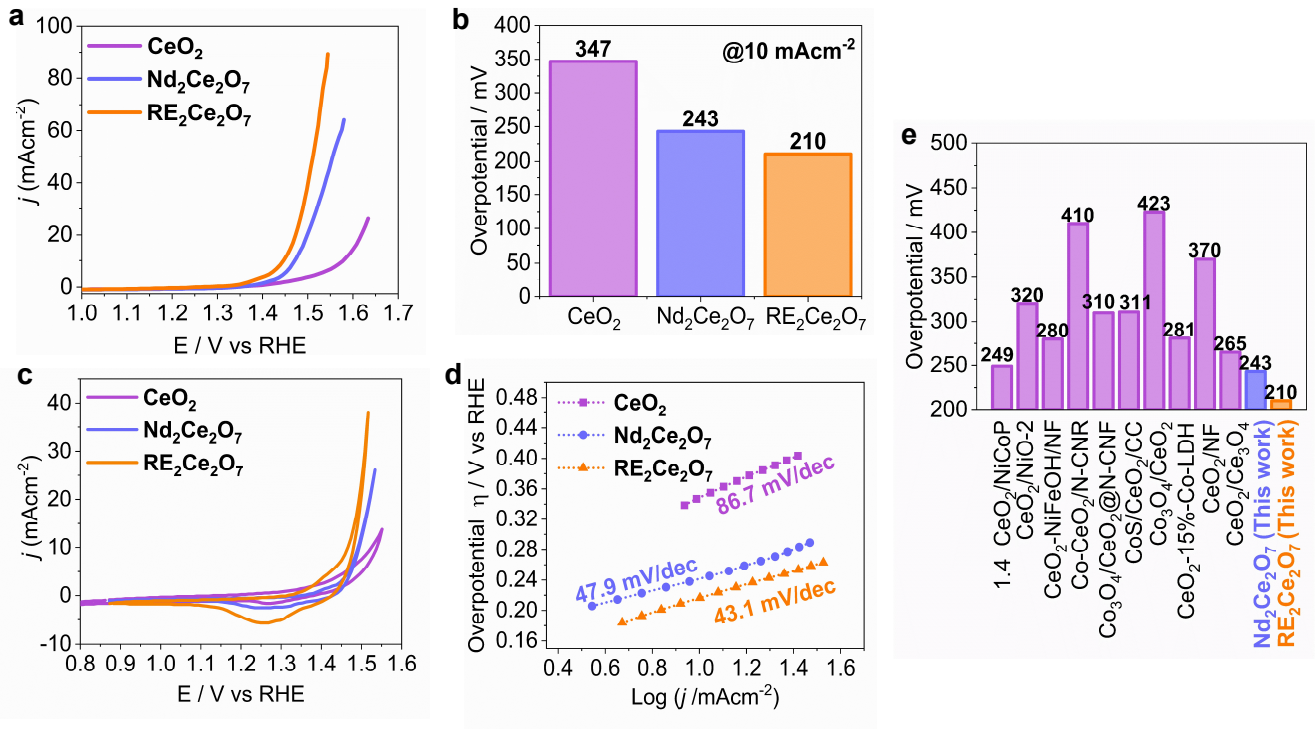

Figure 4 Electrocatalytic performance of CeO_2 (purple), $Nd_2Ce_2O_7$ (blue) and $RE_2Ce_2O_7$ (purple) calcined at 600°C: (a) LSVs measured in N_2 saturated 1 M KOH at a scan rate of 10 mV s^{-1}, (b) overpotential at a current density of 10 mA cm^{-2}, (c) cyclic voltammograms measured in N_2 saturated 1 M KOH at a scan rate of 10 mV s^{-1}, (d) Tafel plots and (e) overpotential benchmark at 10 mA cm^{-2} for recent reports on CeO_2 –based catalysts compared to $RE_2Ce_2O_7$.[50,58,68–74]

achieved the smallest Tafel slope of 43.1 mV dec^{-1}, demonstrating improved OER performance. Tafel slopes for $Nd_2Ce_2O_7$ and CeO_2 were observed to be 49.9 mV dec^{-1} and 86.7 mV dec^{-1} respectively. Thus, the intrinsic activity of the catalysts based on the Tafel slope, follows the order $RE_2Ce_2O_7$ (43.1 mV dec^{-1}) > $Nd_2Ce_2O_7$ (49.9 mV dec^{-1}) > CeO_2 (86.7 mV dec^{-1}). The OER performance of $RE_2Ce_2O_7$ and $Nd_2Ce_2O_7$ reported herein outperform previously reported CeO_2-based electrocatalysts, some of which are summarized as shown in Figure 4(e), demonstrating that RE incorporation can enhance the performance of fluorite OER electrocatalysts.[50,58,68–74] The computed mass activities and turn over frequency (TOF) (at η = 310 mV) are additional parameters employed to probe catalytic OER performance (Figure 5 (a), 5 (b)).

The $RE_2Ce_2O_7$ catalyst demonstrates the best OER activity as it exhibits the highest mass activity and TOF of 47.1 A g^{-1} and 0.0841 s^{-1} respectively. The second-best performance was displayed by $Nd_2Ce_2O_7$ with a mass activity of 23.3 A g^{-1} and TOF of 0.0841 s^{-1}, while CeO_2 showed the weakest performance in this sample series towards OER. The superior intrinsic catalytic activity of $RE_2Ce_2O_7$ relative to the other fluorite catalysts may be explained by the increased number of catalytically active sites, the increase in electronic structure perturbation and oxygen vacancy formation resulting from incorporation of multiple RE cations.[75] To further elucidate the observed enhancement in OER performance resulting from RE incorporation in fluorite catalysts, the electrochemically active surface areas (ECSAs) of the

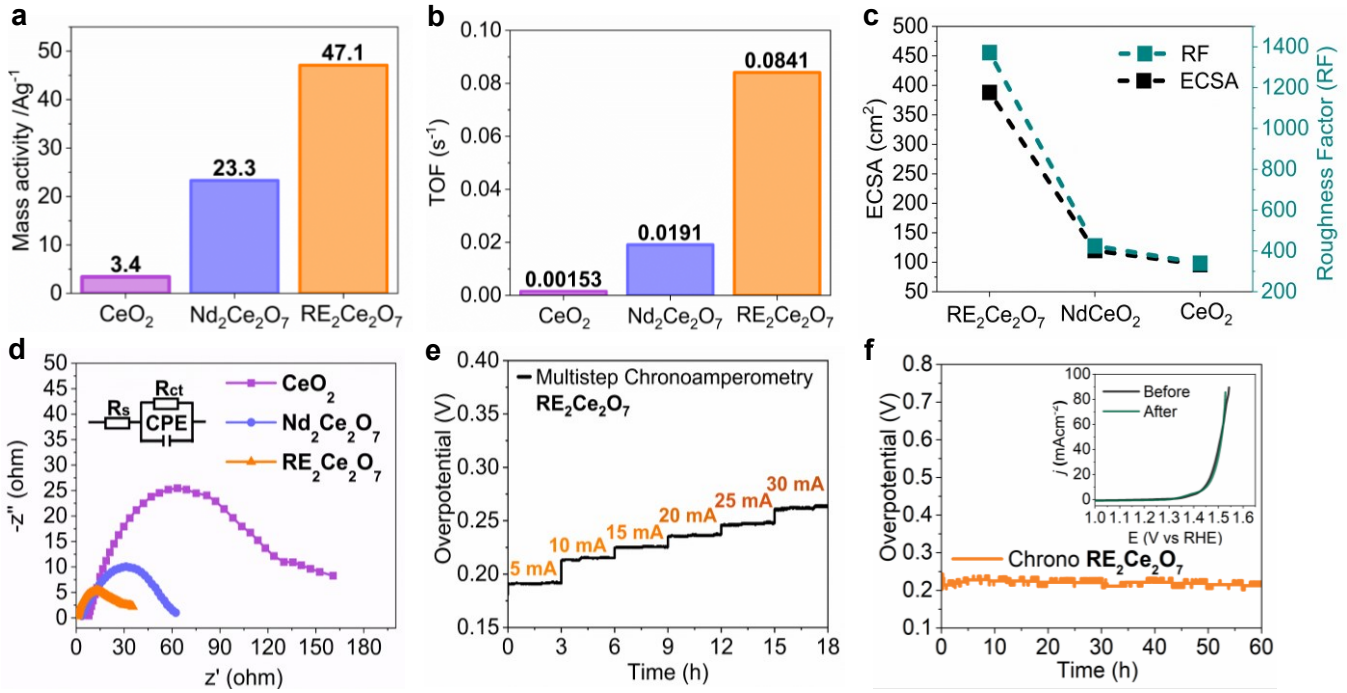

Figure 5 Electrocatalytic performance of CeO_2 (purple), $Nd_2Ce_2O_7$ (blue) and $RE_2Ce_2O_7$ (orange) calcined at 600°C: (a) mass activity, (b) turnover frequency (TOF), (c) electrochemically active surface area (ECSA) shown in black and roughness factor (RF) shown in green and (d) Nyquist plots in the AC frequency range between 100 kHz and 0.1 Hz at 0.55 V; (e) multistep chronoamperometry study of $RE_2Ce_2O_7$ at various current densities and (f) chronoamperometric stability of $RE_2Ce_2O_7$ at a current density of 10 $mAcm^{-2}$ for 60h, where the inset displays OER polarization plots of $RE_2Ce_2O_7$ before and after chronoamperometry.

catalysts was determined from specific electrochemical double-layer capacitance (Cdl) by carrying out CV within a region of non-Faradaic current at varying scan rates (2.5–50 mV s^{-1}) shown in (SI Figures S11-13).

The ECSA and roughness factor were computed (SI Equations S7, S8) as shown in Figure 5 (c). $RE_2Ce_2O_7$ exhibited the largest ECSA, likely due to its highly nanocrystalline nature as evidenced by XRD and SEM analysis. CeO_2 presented the lowest ECSA due its more crystalline morphology. The largest ECSA and highest activity of the $RE_2Ce_2O_7$ sample relative to the other fluorite samples emphasizes the role of morphology on OER activity. ECSA refers to the portion of the electrode surface that actively participates in the electrochemical reaction, such as OER. Thus a large ECSA translates to a larger number of exposed electrochemically active sites, facilitating electrolyte infiltration and surface interaction with the electrocatalyst,[52] leading to exceptional activity toward OER with no hinderance of mass transfer in the electrolyte.[76]

Electrochemical impedance spectroscopy (EIS) analysis reveals the influence of electrical resistivity on OER activity. The EIS spectra of the samples show semicircular curves, indicating electron transfer coupled with the double-layer charging process. The generated Nyquist plots evaluated at 1.55 V vs RHE are shown in Figure 5 (d). The equivalent circuit, shown in the inset, was comprised of the electrolyte resistance (Rs), charge transfer resistance (Rct), and constant phase element (CPE) (SI Table S9). All samples displayed a decrease in conductivity due to reduced interfacial contact from the use of polymer binders to adhere the catalysts to the substrate. However, $RE_2Ce_2O_7$ was found to have the least charge-transfer resistance (Rct) of 3.02 Ω at a potential of 1.55 V (vs RHE), while $Nd_2Ce_2O_7$ and CeO_2 showed a resistance of 7.95 Ω and 18.10 Ω respectively. Thus $RE_2Ce_2O_7$ demonstrates the fastest charge transfer electrokinetics between the electrocatalyst surface and electrolyte solution in the OER. The multistep stability performance of the best catalyst, $RE_2Ce_2O_7$, was measured at different currents (5-30 mA) (Figure 5(e)) and measured at a constant potential, maintained for 60 h (Figure 5(f)). The

multistep stability performance and stability under a constant potential for 16 h of the other catalysts in the sample series is displayed in SI Figure S14.
The results indicate the robustness of $RE_2Ce_2O_7$ both for long term stability and at varying currents at multiple stages, with no rapid degradation of the catalyst. In addition, $Nd_2Ce_2O_7$ and CeO_2 show decent stability with no clear degradation, suggesting their robustness for the OER. Achieving a higher valence state is an essential step to initiating the formation of active M−OOH* species for OER.[77] Surface oxygen vacancies are known to accommodate hydroxyls, consequently enhancing pre-oxidation of low oxidation species, and enabling deprotonation/reconstruction of intermediate species.[78] As exposed RE sites exhibit improved electrophilicity, hydroxyl adsorption onto Ce active sites can be facilitated by oxygen vacancies (V_O) to generate adsorbed M−OH* intermediate species and thereafter instigate the deprotonation step at a minimal potential to generate active oxygen species (RE−OOH*) on the catalyst surface, which justifies the observed enhancement in OER activity.
To examine the behavior of catalysts pre-oxidation during OER, CV was employed. During OER, the pre-oxidation peak of the catalyst as demonstrated by the CV plots becomes more pronounced at higher scan rates (SI Figure S10). $Nd_2Ce_2O_7$ and CeO_2 exhibit one oxidation and one reduction peak at all scan rates. With varying scan rate from 2.5-100 mV/s, both $Nd_2Ce_2O_7$ and CeO_2, show a shift in oxidation peak to a higher potential and a shift in reduction peak to a lower potential. This suggests that the redox processes in $Nd_2Ce_2O_7$ are similar to those in CeO_2. However, $RE_2Ce_2O_7$ exhibits two distinct reduction peaks and one oxidation peak shoulder, suggesting a unique redox process for the CCO catalyst. The difference in redox behavior of $RE_2Ce_2O_7$ can be attributed to the pre-oxidation of Ce and other RE metal ions present in this composition. Ce ions may be the main active site while other ions play a supporting role in modulating its electronic/structural configuration, thereby significantly boosting its electrocatalytic performance towards OER. The electrochemical OER parameters of CeO_2, $Nd_2Ce_2O_7$ and $RE_2Ce_2O_7$ electrocatalysts are compared in Table 1. $RE_2Ce_2O_7$ shows the lowest overpotential and Tafel slope, indicating the best activity. Furthermore, the obtained TOF, mass activity and ECSA for $RE_2Ce_2O_7$ were highest among the fluorite sample series, further corroborating its exceptional performance. Higher ECSA value generally indicates larger electrochemically active surface area which improves electrolyte/active sites interaction, leading to better catalytic performance for OER. Large ECSA value results in high surface roughness (RF), which is another parameter examined, that affects catalytic activity.

Table 1 Catalytic performance of fluorite catalysts.

	CeO_2	$Nd_2Ce_2O_7$	$RE_2Ce_2O_7$
Onset potential (V)	1.52	1.41	1.38
Overpotential @ 10 mA cm^{-2} (mV)	347	243	210
$Ce^{3+} \rightarrow Ce^{4+}$ oxidation peak potential (V)	1.38	1.35	1.43
TOF	0.0015	0.0191	0.0841
Mass Activity	3.43	23.26	47.09
Tafel slope (mV $deccm^{-1}$	86.7	47.9	43.1
ECSA (cm^2)	96	120	388
RF	340	425	1372

It is our understanding that the exceptional catalytic performance of our novel $RE_2Ce_2O_7$ catalyst can primarily be attributed to improvements in charge and mass transfer. The abundant oxygen vacancy defects in $RE_2Ce_2O_7$ enhances the OER electrokinetics, while the incorporation of RE elements into the CeO_2 lattice provides suitable electronic structure. Furthermore, the mesoporous and nanostructured nature of the $RE_2Ce_2O_7$ sample substantially minimizes the bubbles/electrode contact region, which facilitates the bubble release and reactant transfer. In addition, the lattice expansion and local atomic disorder resulting from RE incorporation, increases the number of active sites as well as electron transport conductivity from the surface of the catalyst.
The long-term chronoamperometric stability of CeO_2 and $Nd_2Ce_2O_7$ for 16h and $RE_2Ce_2O_7$ for 60h (SI Figure S14, Figure 5 (f) respectively) indicate robust catalytic stability with no significant deterioration

under uninterrupted OER conditions at constant potentials of 1.46, 1.52 and 1.65 V respectively. The OER polarization plot of $RE_2Ce_2O_7$ before and after the stability study shows no observable changes as displayed by the inset in Figure 5 (f), demonstrating the excellent mass transfer property and mechanical ruggedness of the $RE_2Ce_2O_7$ electrode in an alkaline environment. Following stability measurements, analysis of the catalyst surface of the best performing catalyst $RE_2Ce_2O_7$ using Raman and analysis of the bulk of the catalyst using powder XRD, revealed no new phase formation on the catalyst surface as seen in SI Figures S15 and S16 respectively. Additionally, CeO_2 and $Nd_2Ce_2O_7$ were also found to exhibit stability in an alkaline medium as evidenced by similar Raman spectra before and after OER. Furthermore, XPS analysis of all samples after carrying out stability measurements are shown in SI Figures S17–S19. XPS results show no significant changes in surface electronic states of the elemental compositions of the catalysts before and after stability measurement for all samples indicating that the integrity of the catalysts is retained. In addition, the O1s spectrum of $RE_2Ce_2O_7$ (SI Figure S17 (h))shows the presence of both chemically and physically adsorbed OH after activity, demonstrating the quick adsorption of OH on the surface, consistent with its characteristic large surface area and high concentration of oxygen vacancies and active sites.

Finally, the CCO-modified electrode was tested as both cathode and anode catalyst in a full water electrolyzer set-up, as shown in SI Figure S20. A two-electrode configuration was used, and a current density of $\sim$20 mA/cm^2 was achieved with a cell potential of $\sim$1.5V in a 0.3/1.0 M KOH electrolyte. Achieving such low water splitting voltage is significantly more efficient compared to electrolyzers employing precious metal based electrocatalysts, e.g. Pt$||RuO_2$, and further highlights the efficacy of these CCO-based electrocatalysts.

3 Conclusion

In this work, EISA derived CeO_2, $Nd_2Ce_2O_7$, and CCO $RE_2Ce_2O_7$ high surface area nanocatalysts are studied to understand the impact of calcination temperature and extent of compositional complexity on OER electrocatalytic activity and stability. Among the various calcination temperatures investigated, fluorite compositions calcined at 600°C were found to exhibit the optimal catalytic activity for the OER. CCO $RE_2Ce_2O_7$ synthesized at 600°C outperforms some of the best OER catalysts including RuO_2, IrO_2 and NiO_x.[79] Additionally, chronoamperometry stability measurements in an alkaline environment reveal that $RE_2Ce_2O_7$ displays long term stability with no evidence of degradation.

A combination of long range and short range structural probes reveals the inclusion of mainly RE^{3+} cations in the fluorite lattice results in the formation of Frenkel defects and a partially reduced defect phase with local and long-range oxygen vacancy ordering ($RE_{1.5}Ce_{1.5}O_{5+x}$) to maintain charge balance. While inclusion of Nd (a single RE^{3+} cation) was found to induce these effects and improve OER activity, the compositionally complex $RE_2Ce_2O_7$ catalyst displayed the highest extent of vacancy ordering and best OER activity. The superior intrinsic catalytic activity of $RE_2Ce_2O_7$ relative to the other fluorite catalysts in this series, may be attributed to an increase in: (i) number of catalytically active sites, (ii) electronic structure perturbation and (iii) concentration of oxygen Frenkel defects and presence of $RE_{1.5}Ce_{1.5}O_{5+x}$ defect phase resulting from the incorporation of multiple RE cations. The larger concentration of surface oxygen vacancies in $RE_2Ce_2O_7$ facilitates the pre-oxidation of RE sites, increases hydroxyl adsorption and promotes the reconstruction of the defective surface with applied potential. In addition to an improvement in intrinsic catalytic activity, the large surface area resulting from the nanoarchitecture of the $RE_2Ce_2O_7$ catalyst plays a key role in improving OER activity by increasing the number of exposed electrochemically active sites, facilitating electrolyte infiltration and surface interaction with the electrocatalyst. Overall, this work demonstrates that a CCO configuration expands abilities to tailor fluorite nanocatalysts. Further investigation is warranted to determine the role of the nature of RE cations and varying number of RE cations on the OER activity of fluorite nanocatalysts.

4 Experimental Section

4.1 Materials

Praseodymium (III) nitrate pentahydrate (99.9%), cerium (III) nitrate hexahydrate (99.5%), terbium (III) nitrate hydrate (99.9%), lanthanum (III) nitrate hexahydrate (98%), dysprosium (III) nitrate pentahydrate (99.9%), neodymium (III) nitrate hexahydrate (99.9%) and ethanol (99.5%) were purchased from Thermo Fisher Scientific. Pluronic P123 (a symmetric triblock copolymer comprising poly(ethylene oxide) (PEO) and poly(propylene oxide) (PPO) in an alternating linear fashion) was purchased from Sigma Aldrich. All metal nitrates were used to prepare sealed aqueous stock solutions immediately upon receipt from the manufacturer.
Carbon cloth for the battery, fuel cell and supercapacitor was purchased from MSE supplies. Nafion (5 %) and isopropanol (iPr-OH), were purchased from Sigma–Aldrich and sodium hydroxide was purchased from Fisher Scientific and these reagents were used as received. Deionized (D.I) water purified through a Millipore system was used in all experiments. The CC was washed with iPr-OH and D.I water several times to ensure the surface was clean before use.

4.2 Material Synthesis

4.2.1 Synthesis of Mesoporous Fluorite's via Evaporation Induced Self Assembly (EISA)

Mesoporous fluorite compositions were synthesized using a soft templating approach via evaporation induced self-assembly, as illustrated in Figure 1.Briefly, metal nitrate precursor solutions were dissolved in ethanol, under continuous stirring, using Pluronic P123 as a block copolymer template. The solutions were allowed to evaporate in a petri dish at room temperature for 48 hours and the resulting gels were calcined in air at 400 °C, 600 °C, 800 °C or 1000 °C for 4 hours in an oven. The following compositions were chosen to investigate the role of RE cations and compositional complexity on the electrochemical OER performance of fluorites: $(La_{0.2}Pr_{0.2}Nd_{0.2}Tb_{0.2}Dy_{0.2})_2Ce_2O_7$, $Nd_2Ce_2O_7$ and CeO_2. $(La_{0.2}Pr_{0.2}Nd_{0.2}Tb_{0.2}Dy_{0.2})_2Ce_2O_7$ is referred to as $RE_2Ce_2O_7$ in this study.

4.2.2 Fabrication of the Working Electrode for OER

All carbon cloth substrates were cleaned using iPr-OH, dried and covered with Teflon tape, leaving an exposed geometric area of 0.283 cm^2. Catalyst ink was prepared by dispersing 10.0 mg of the catalyst in 1.0 mL 0.8% Nafion in iPr-OH and ultrasonicated for 30 min. A 20 μL volume of the ink was drop-casted on the exposed area of the CC substrate, dried at room temperature, and finally heated at 130°C in an oven for 30 min in air to obtain the working electrode.

4.3 Structural Characterization

Phase identification of the as synthesized fluorite powder samples was performed using a Panalytical Empyrean laboratory powder X-ray diffraction (XRD) instrument with Cu Kα radiation (λ = 1.5418 Å). Rietveld refinements were performed on the XRD data using the TOPAS v6 software.[80] Data were fit to a tetragonal unit cell model with S.G. $P4_2/nmc$ for CeO_2 and a cubic defect fluorite unit cell model with S.G. $Fm\bar{3}m$ for $Nd_2Ce_2O_7$ and $RE_2Ce_2O_7$. Lattice parameter(s), isotropic atomic displacement and Scherrer particle size parameters were refined. $Nd_2Ce_2O_7$ calcined at 1000°C was fit to a cubic C-type (bixbyite) structure and refined similarly. The chemical homogeneity of the samples was investigated by performing EDS measurements on pressed pellets of the fluorite CCOs using a Zeiss EVO SEM equipped with energy dispersive X-Ray Spectroscopy. BET surface area measurements were performed by loading 100mg - 150mg of powder sample in a glass tube and out gassing overnight at 200°C in vacuum. The outgassed samples were then measured using a Micromeritics Gemini VII surface-area analyzer. XPS measurements were performed using a KRATOS AXIS 165 X-ray photoelectron spectrometer (Kratos Analytical Limited, Manchester, United Kingdom) using a monochromatic Al X-ray source. The C 1s signal at 284.5 eV was used as a reference to correct all the XPS binding energies. Neutron powder diffraction (NPD) and atomic pair distribution function (PDF) data were collected at 300 K on the Nanoscale Ordered Materials Diffractometer (NOMAD) at the Spallation Neutron Source (SNS) at Oak Ridge National Laboratory (ORNL).[81] 100mg of each sample was loaded into a 3 mm diameter quartz capil-

lary, placed in a temperature controlled Ar cryostream, and data were collected for 1 h. Signals from the empty quartz capillary and instrument were collected to facilitate background subtraction from the sample data. Data reduction was completed using the Advanced Diffraction Environment (ADDIE) suite and a $Q_{max}$of 25 $Å^{-1}$ and a Lorch filter was applied for PDF generation.[82] The data was corrected for detector deadtime, absorption, and multiple scattering effects, and subsequently normalized by the incident flux and total scattering cross section of the sample. Rietveld refinements of the neutron diffraction data were performed using TOPAS v6 software[80] and PDF analysis was completed using the PDFgui software package.[83] Rietveld refinement of time-of-flight neutron diffraction data for CeO_2 was performed using S.G. $P4_2/nmc$ while $Nd_2Ce_2O_7$ and $RE_2Ce_2O_7$ were refined using a two phase structural model comprising of a primary phase with S.G. $Fm\bar{3}m$ containing oxygen Frenkel defects and a secondary phase with S.G. $Pnn2$ containing oxygen vacancy ordering. For all samples, lattice parameter(s), isotropic atomic displacement and oxygen occupancy were refined. The same average structure models for $Nd_2Ce_2O_7$ and $RE_2Ce_2O_7$ were applied to PDF analysis and most parameters were fixed, while lattice parameter a was refined. PDF analysis for CeO_2 was performed using a two phase structural model comprising of a primary phase with S.G. $P4_2/nmc$ containing oxygen Frenkel defects and a secondary phase with S.G. $Pnn2$ containing oxygen vacancy ordering. Lattice parameters, isotropic atomic displacement and oxygen occupancy were refined. All XPS spectra were collected from the pristine catalyst surface without sputtering. The Raman spectra of the catalyst were recorded with LabRam ARAMIS (HORIBA Jobin-Yvon Raman spectrometer equipped with a CCD detector) in the Raman shift range between 50 cm^{-1} to 1800 cm^{-1}, 1200 lines mm^{-1} grating, HeNe laser 632.8 nm excitation with a nominal output power of 100mW, 0.95 cm^{-1}/pixel spectral dispersion, 10% of laser power, 10x objective, 0.25 numerical aperture, 100 μm slit, 200 μm hole, 30 seconds exposure time, and 10x accumulations for each sample acquisition.[84]

4.4 Electrochemical Measurements

Electrochemical measurements were performed using a conventional three-electrode system connected to an IviumStat potentiostat, with the fluorite catalyst as the working electrode, while graphite rod and Ag/AgCl electrode were used as counter electrode and reference electrodes respectively, to measure the electrocatalytic performances. Linear sweep voltammetry (LSV), and cyclic voltammetry (CV) were carried out to study the OER catalytic performance and cycling stability. In order to reduce uncompensated solution resistance, all activity data were iR corrected, which was measured through electrochemical impedance studies. All potentials measured were calibrated to a reversible hydrogen electrode (RHE) using SI Equation S1. All electrolytes were saturated by oxygen (for OER) bubbles before and during the experiments.

The steady-state performance and durability of all the electrocatalysts in OER for long-term chronoamperometric stability in an alkaline electrolyte of 1 M KOH solution was carried out in two forms: (a) at constant current density of 20 mA cm^{-2} for 24 h, (b) for $RE_2Ce_2O_7$, various current densities between 5 – 30 mA cm^{-2} as multistep study, in N_2-saturated 1.0 M KOH at room temperature.

The Tafel slope, which is an important parameter associated with catalytic activity and reaction rate of these catalysts for OER, was estimated from a Tafel plot with the equation shown in SI Equation S2.

The Electrochemical Impedance Spectroscopy (EIS) experiments were performed within $10^5 - 10^{-2}$ Hz frequency range, at an AC signal amplitude of 10 mV, to study the electrode kinetics and estimate the electrolyte resistance (Rs), and charge transfer resistance at the electrode (catalyst)-electrolyte interface (Rct). The Nyquist plots were collected in N_2-saturated 1.0 M KOH at an applied potential of 0.55 V vs. Ag|AgCl (KCl saturated).

Turnover frequency (TOF), mass activity, electrochemically active surface area (ECSA) and roughness factor (RF), which are parameters used to evaluate the electrocatalytic performance of catalysts for the OER, were determined for the fluorite samples as shown in SI Equations S3-S8.

Supporting Information

Supporting Information is available from the Wiley Online Library or from the author.

Acknowledgements

The material synthesis efforts in this work were supported by the donors of ACS Petroleum Research Fund under Doctoral New Investigator Grant 62728-DNI3. Material characterization efforts were supported by the National Science Foundation under NSF-DMR-2145174. XRD measurements were completed at the Diffraction Facility at the Institute for Advanced Materials and Manufacturing at the University of Tennessee. This research used beamline BL-1B (NOMAD) at the Spallation Neutron Source, a DOE Office of Science User Facility operated by the Oak Ridge National Laboratory.

Notes and references

[1] H. B. Gray, *Nature Chemistry* **2009**, *1*, 1 7.

[2] W. Li, D. Xiong, X. Gao, L. Liu, *Chem. Commun.* **2019**, *55*, 60 8744.

[3] J. A. Dias, M. A. S. Andrade Jr, H. L. S. Santos, M. R. Morelli, L. H. Mascaro, *ChemElectroChem* **2020**, *7*, 15 3173.

[4] B. H. R. Suryanto, Y. Wang, R. K. Hocking, W. Adamson, C. Zhao, *Nature Communications* **2019**, *10*, 1 5599.

[5] X. Z. Song, W. Y. Zhu, X. F. Wang, Z. Tan, *ChemElectroChem* **2021**, *8*, 6 996.

[6] Q. Li, L. Song, Z. Liang, M. Sun, T. Wu, B. Huang, F. Luo, Y. Du, C.-H. Yan, *Advanced Energy and Sustainability Research* **2021**, *2*, 2 2000063.

[7] S. Anantharaj, S. R. Ede, K. Sakthikumar, K. Karthick, S. Mishra, S. Kundu, *ACS Catalysis* **2016**, *6*, 12 8069.

[8] Q. Shi, C. Zhu, D. Du, Y. Lin, *Chem. Soc. Rev.* **2019**, *48*, 12 3181.

[9] N.-T. Suen, S.-F. Hung, Q. Quan, N. Zhang, Y.-J. Xu, H. M. Chen, *Chem. Soc. Rev.* **2017**, *46*, 2 337.

[10] L. Xu, Q. Jiang, Z. Xiao, X. Li, J. Huo, S. Wang, L. Dai, *Angewandte Chemie International Edition* **2016**, *55*, 17 5277.

[11] L. C. Seitz, C. F. Dickens, K. Nishio, Y. Hikita, J. Montoya, A. Doyle, C. Kirk, A. Vojvodic, H. Y. Hwang, J. K. Norskov, T. F. Jaramillo, *Science* **2016**, *353*, 6303 1011.

[12] S. Park, Y. Shao, J. Liu, Y. Wang, *Energy Environ. Sci.* **2012**, *5*, 11 9331.

[13] F. Esch, S. Fabris, L. Zhou, T. Montini, C. Africh, P. Fornasiero, G. Comelli, R. Rosei, *Science* **2005**, *309*, 5735 752.

[14] M. Coduri, S. Checchia, M. Longhi, D. Ceresoli, M. Scavini, *Frontiers in Chemistry* **2018**, *6*.

[15] U. Aarthi, D. Shukla, S. Rengaraj, K. S. Babu, *Journal of Alloys and Compounds* **2020**, *838* 155534.

[16] K. Zhu, F. Shi, X. Zhu, W. Yang, *Nano Energy* **2020**, *73* 104761.

[17] E. Marelli, J. Gazquez, E. Poghosyan, E. Müller, D. J. Gawryluk, E. Pomjakushina, D. Sheptyakov, C. Piamonteze, D. Aegerter, T. J. Schmidt, M. Medarde, E. Fabbri, *Angewandte Chemie International Edition* **2021**, *60*, 26 14609.

[18] Y. Xiao, Y. Wang, M. Xiao, C. Liu, S. Hou, J. Ge, W. Xing, *NPG Asia Materials* **2020**, *12*, 1 73.

[19] M. Brahlek, M. Gazda, V. Keppens, A. R. Mazza, S. J. McCormack, A. Mielewczyk-Gryń, B. Musico, K. Page, C. M. Rost, S. B. Sinnott, C. Toher, T. Z. Ward, A. Yamamoto, *APL Materials* **2022**, *10*, 11 110902.

[20] A. J. Wright, J. Luo, *Journal of Materials Science* **2020**, *55*, 23 9812.

[21] M. Qin, H. Vega, D. Zhang, S. Adapa, A. J. Wright, R. Chen, J. Luo, *Journal of Advanced Ceramics* **2022**, *11*, 4 641.

[22] D. Zhang, H. A. De Santiago, B. Xu, C. Liu, J. A. Trindell, W. Li, J. Park, M. A. Rodriguez, E. N. Coker, J. D. Sugar, A. H. McDaniel, S. Lany, L. Ma, Y. Wang, G. Collins, H. Tian, W. Li, Y. Qi, X. Liu, J. Luo, *Chemistry of Materials* **2023**, *35*, 5 1901.

[23] M.-J. Choi, L. Wang, K. A. Stoerzinger, S.-Y. Chung, S. A. Chambers, Y. Du, *Advanced Energy Materials* **2023**, 2300239.

[24] C. Duan, X. Li, D. Wang, Z. Wang, H. Sun, R. Zheng, Y. Liu, *Sustainable Energy Fuels* **2022**, *6*, 6 1479.

[25] Y.-R. Zheng, M.-R. Gao, Q. Gao, H.-H. Li, J. Xu, Z.-Y. Wu, S.-H. Yu, *Small* **2015**, *11*, 2 182.

[26] J. W. D. Ng, M. García-Melchor, M. Bajdich, P. Chakthranont, C. Kirk, A. Vojvodic, T. F. Jaramillo, *Nature Energy* **2016**, *1*, 5 16053.

[27] T. Odedairo, X. Yan, X. Yao, K. K. Ostrikov, Z. Zhu, *Advanced Materials* **2017**, *29*, 46 1703792.

[28] D. Briggs, *Surface and Interface Analysis* **1981**, *3*, 4.

[29] H. Brunckova, H. Kolev, M. Kanuchova, *Surface and Interface Analysis* **2019**, *51*, 3 326.

[30] J. P. Baltrus, M. J. Keller, *Surface Science Spectra* **2019**, *26*, 1 14001.

[31] V. Tangoulis, N. Lalioti, J. Parthenios, N. Boukos, O. Malina, J. Tuček, R. Zbořil, *Inorganic Chemistry* **2018**, *57*, 11 6391.

[32] E. Mamontov, T. Egami, R. Brezny, M. Koranne, S. Tyagi, *Journal of Physical Chemistry B* **2000**, *104*, 47 11110.

[33] R. Schmitt, A. Nenning, O. Kraynis, R. Korobko, A. I. Frenkel, I. Lubomirsky, S. M. Haile, J. L. Rupp, *Chemical Society Reviews* **2020**, *49*, 2 554.

[34] J. A. Lussier, D. H. P. Souza, P. S. Whitfield, M. Bieringer, *Inorganic Chemistry* **2018**, *57*, 22 14106.

[35] T. Hagiwara, Z. Kyo, A. Manabe, H. Yamamura, K. Nomura, *Journal of the Ceramic Society of Japan* **2009**, *117* 1306.

[36] U. Aarthi, D. Shukla, S. Rengaraj, K. S. Babu, *Journal of Alloys and Compounds* **2020**, *838* 155534.

[37] L.-E. Kalland, A. Løken, T. S. Bjørheim, R. Haugsrud, T. Norby, *Solid State Ionics* **2020**, *354* 115401.

[38] J. Ibáñez, J. Á. Sans, V. Cuenca-Gotor, R. Oliva, Ó. Gomis, P. Rodríguez-Hernández, A. Muñoz, U. Rodríguez-Mendoza, M. Velázquez, P. Veber, C. Popescu, F. J. Manjón, *Inorganic Chemistry* **2020**, *59*, 14 9648.

[39] R. D. Shannon, C. T. Prewitt, *Acta Crystallographica Section B* **1969**, *25*, 5 925.

[40] R. D. Shannon, *Acta Crystallographica Section A* **1976**, *32*, 5 751.

[41] Carmelo Giacovazzo, Hugo Luis Monaco, Gilberto Artioli, Davide Viterbo, Marco Milanesio, Gastone Gilli, Paola Gilli, Giuseppe Zanotti, Giovanni Ferraris, M. Catti, C. Giacovazzo, *Acta Crystallographica Section A* **1993**, *49* 373.

[42] H. Nitani, T. Nakagawa, M. Yamanouchi, T. Osuki, M. Yuya, T. A. Yamamoto, *Materials Letters* **2004**, *58*, 15 2076.

[43] A. E. Baranchikov, O. S. Polezhaeva, V. K. Ivanov, Y. D. Tretyakov, *CrystEngComm* **2010**, *12*, 11 3531.

[44] S. A. Deshpande, S. D. Patil, S. V. Kuchibhatla, S. Seal, *Applied Physics Letters* **2005**, *87* 133113.

[45] L. Chen, P. Fleming, V. Morris, J. D. Holmes, M. A. Morris, *The Journal of Physical Chemistry C* **2010**, *114*, 30 12909.

[46] L. Cong, S. Zhang, S. Gu, W. Li, *Journal of Materials Science and Technology* **2021**, *85* 152.

[47] Z. Wu, M. Li, J. Howe, H. M. Meyer, S. H. Overbury, *Langmuir* **2010**, *26*, 21 16595.

[48] J. E. Spanier, R. D. Robinson, F. Zhang, S.-W. Chan, I. P. Herman, *Phys. Rev. B* **2001**, *64*, 24 245407.

[49] T. Taniguchi, T. Watanabe, N. Sugiyama, A. K. Subramani, H. Wagata, N. Matsushita, M. Yoshimura, *The Journal of Physical Chemistry C* **2009**, *113*, 46 19789.

[50] D. Ghosh, M. Manikanta Kumar, C. R. Raj, D. Pradhan, *ACS Applied Energy Materials* **2022**, *5*, 5 5666.

[51] A. Nakajima, A. Yoshihara, M. Ishigame, *Phys. Rev. B* **1994**, *50*, 18 13297.

[52] K. Liu, Z. Zhu, M. Jiang, L. Li, L. Ding, M. Li, D. Sun, G. Yang, G. Fu, Y. Tang, *Chemistry – A European Journal* **2022**, *28*, 32 e202200664.

[53] S. Paladugu, P. C. Metz, S. Luo, M. Li, J. Liu, H. I. I. I. Meyer, Y. Wu, Z. Wu, K. Page, *The Journal of Physical Chemistry C* **2023**, *127*, 7 3689.

[54] T. X. Nguyen, Y.-C. Liao, C.-C. Lin, Y.-H. Su, J.-M. Ting, *Advanced Functional Materials* **2021**, *31*, 27 2101632.

[55] S. Nundy, D. Tatar, J. Kojčinović, H. Ullah, A. Ghosh, T. Mallick, R. Meinusch, B. Smarsly, A. Tahir, I. Djerdj, *Advanced Sustainable Systems* **2022**, *6*.

[56] K. I. Maslakov, Y. A. Teterin, A. J. Popel, A. Y. Teterin, K. E. Ivanov, S. N. Kalmykov, V. G. Petrov, R. Springell, T. B. Scott, I. Farnan, *Applied Surface Science* **2018**, *433* 582.

[57] Y. Zhu, N. Jain, M. Hudait, D. Maurya, R. Varghese, S. Priya, *Journal of vacuum science & technology. B, Microelectronics and nanometer structures: processing, measurement, and phenomena: an official journal of the American Vacuum Society* **2014**, *32* .

[58] B. Qiu, C. Wang, N. Zhang, L. Cai, Y. Xiong, Y. Chai, *ACS Catalysis* **2019**, *9*, 7 6484.

[59] F. H. Aragón, I. Gonzalez, J. A. H. Coaquira, P. Hidalgo, H. F. Brito, J. D. Ardisson, W. A. A. Macedo, P. C. Morais, *The Journal of Physical Chemistry C* **2015**, *119*, 16 8711.

[60] D. D. Koelling, A. M. Boring, J. H. Wood, *Solid State Communications* **1983**, *47*, 4 227.

[61] G. Blanco, J. M. Pintado, S. Bernal, M. A. Cauqui, M. P. Corchado, A. Galtayries, J. Ghijsen, R. Sporken, T. Eickhoff, W. Drube, *Surface and Interface Analysis* **2002**, *34*, 1 120.

[62] Y. Zhao, J.-G. Li, M. Guo, X. Yang, *J. Mater. Chem. C* **2013**, *1*, 22 3584.

[63] Y. Gil, R. C. de Santana, A. S. S. de Camargo, L. G. Merízio, P. F. Carreño, P. Fuentealba, J. Manzur, E. Spodine, *Dalton Trans.* **2023**, *52*, 10 3158.

[64] B. Hua, Y.-Q. Zhang, N. Yan, M. Li, Y.-F. Sun, J. Chen, J. Li, J.-L. Luo, *Advanced Functional Materials* **2016**, *26*, 23 4106.

[65] L. Tang, Y. Yang, H. Guo, Y. Wang, M. Wang, Z. Liu, G. Yang, X. Fu, Y. Luo, C. Jiang, Y. Zhao, Z. Shao, Y. Sun, *Advanced Functional Materials* **2022**, *32*, 28 2112157.

[66] J. Zhao, C. Liu, J. Li, R. Wu, J. Wang, H. Qian, H. Guo, J. Li, K. Ibrahim, *AIP Advances* **2019**, *9*, 5 55208.

[67] Y. Zhu, W. Zhou, J. Yu, Y. Chen, M. Liu, Z. Shao, *Chemistry of Materials* **2016**, *28*, 6 1691.

[68] M. Gao, Z. Wang, S. Sun, D. Jiang, M. Chen, *Nanotechnology* **2021**, *32*, 19 195704.

[69] H. Xie, Q. Geng, X. Liu, J. Mao, *Frontiers of Chemical Science and Engineering* **2022**, *16*, 3 376.

[70] H. Zhang, J. Du, D. Niu, S. Hu, X. Zhang, *International Journal of Electrochemical Science* **2019**, 6532–6545.

[71] A. Sivanantham, P. Ganesan, S. Shanmugam, *Applied Catalysis B: Environmental* **2018**, *237* 1148.

[72] T. Li, S. Li, Q. Liu, Y. Tian, Y. Zhang, G. Fu, Y. Tang, *ACS Sustainable Chemistry & Engineering* **2019**, *7*, 21 17950.

[73] J. Huang, H. Sheng, R. D. Ross, J. Han, X. Wang, B. Song, S. Jin, *Nature Communications* **2021**, *12*, 1 3036.

[74] Y. Li, X. Zhang, Z. Zheng, *Small* **2022**, *18*, 17 2107594.

[75] H. Wang, X. Chen, D. Huang, M. Zhou, D. Ding, H. Luo, *ChemCatChem* **2020**, *12*, 10 2768.

[76] T. Wang, H. Chen, Z. Yang, J. Liang, S. Dai, *Journal of the American Chemical Society* **2020**, *142*, 10 4550.

[77] S. C. Petitto, E. M. Marsh, G. A. Carson, M. A. Langell, *Journal of Molecular Catalysis A: Chemical* **2008**, *281*, 1-2 49.

[78] Z. Xiao, Y.-C. Huang, C.-L. Dong, C. Xie, Z. Liu, S. Du, W. Chen, D. Yan, L. Tao, Z. Shu, G. Zhang, H. Duan, Y. Wang, Y. Zou, R. Chen, S. Wang, *Journal of the American Chemical Society* **2020**, *142*, 28 12087.

[79] A. T. Swesi, J. Masud, M. Nath, *Energy Environ. Sci.* **2016**, *9*, 5 1771.

[80] A. A. Coelho, *Journal of Applied Crystallography* **2018**, *51*, 1 210.

[81] J. Neuefeind, M. Feygenson, J. Carruth, R. Hoffmann, K. K. Chipley, *Nuclear Instruments and Methods in Physics Research Section B: Beam Interactions with Materials and Atoms* **2012**, *287* 68.

[82] M. T. McDonnell, D. P. Olds, K. L. Page, J. C. Neufeind, M. G. Tucker, J. C. Bilheux, W. Zhou, P. F. Peterson, *Acta Crystallographica Section A* **2017**, *A73* a377.

[83] C. L. Farrow, P. Juhas, J. W. Liu, D. Bryndin, E. S. Božin, J. Bloch, T. Proffen, S. J. L. Billinge, *Journal of Physics: Condensed Matter* **2007**, *19*, 33 335219.

[84] I. M. Abdullahi, M. Langenderfer, O. Shenderova, N. Nunn, M. D. Torelli, C. E. Johnson, V. N. Mochalin, *Carbon* **2020**, *164* 442.